3-D X-ray Nanotomography Reveals Different Carbon Deposition Mechanisms in a Single Catalyst Particle

Martin Veselý,[a] Roozbeh Valadian,[a] Leon Merten Lohse,[b] Mareike Toepperwien,[b] Kathryn Spiers,[c] Jan Garrevoet,[c] Eelco T. C. Vogt,[a, d] Tim Salditt,[b] Bert M. Weckhuysen,*[a] and Florian Meirer*[a]

Catalyst deactivation involves a complex interplay of processes taking place at different length and time scales. Understanding this phenomenon is one of the grand challenges in solid catalyst characterization. A process contributing to deactivation is carbon deposition (i.e., coking), which reduces catalyst activity by limiting diffusion and blocking active sites. However, characterizing coke formation and its effects remains challenging as it involves both the organic and inorganic phase of the catalytic process and length scales from the atomic scale to the scale of the catalyst body. Here we present a combination of hard X-ray imaging techniques able to visualize in 3-D the distribution, effect and nature of carbon deposits in the macropore space of an entire industrially used catalyst particle. Our findings provide direct evidence for coke promoting effects of metal poisons, pore clogging by coke, and a correlation between carbon nature and its location. These results provide a better understanding of the coking process, its relation to catalyst deactivation and new insights into the efficiency of the industrial scale process of fluid catalytic cracking.

Introduction

Carbon deposits on catalysts are an unwanted side product of any chemical reaction where hydrocarbons react over heterogeneous catalysts. They can play different roles and are commonly reported to deactivate the catalyst by pore clogging or by covering the catalytically active site.[1–5] These deposits consist of a mixture of different hydrocarbon species, are commonly called 'coke', and have already been the topic of numerous experimental and theoretical investigations for decades. Various analytical methods have been used in the past to study carbon deposits in solid catalysts providing bulk information on both the species and origin of the coke accumulated during catalyst operation. Studies on industrial catalysts are less common; coke in industrial reforming, hydrotreating, or cracking catalysts was studied using solid-state carbon magic angle spinning nuclear magnetic resonance (^{13}C-MAS-NMR),[3,6–11] supercritical fluid extraction (SFE),[3,7] electron paramagnetic resonance (EPR),[12] near-edge X-ray absorption fine structure (NEXAFS),[11,13] X-ray photoelectron spectroscopy (XPS),[7,11] X-ray diffraction (XRD),[14] matrix-assisted laser/desorption ionization time-of-flight mass spectrometry (MALDI-TOF-MS),[6] temperature-programmed hydrogenation (TPH) and oxidation (TPO),[11,15] Raman spectroscopy,[11,14] UV-vis microspectroscopy,[16] proton-induced X-ray emission (PIXE), and nuclear reaction analysis (NRA).[17] These techniques often rely on coke-containing samples from which the catalyst was leached (e.g., by dissolution in hydrofluoric acid[4]) and provide either bulk information or 2-D data at a spatial resolution that is too low to study the relation of catalyst structure and composition on the one hand and coke on the other hand.

In order to reveal the prevailing deactivation mechanism and to quantify the deactivation effect, however, knowledge of the 3-D coke distribution at different length scales is crucial.[18] At the smallest scale, atom probe tomography (APT) has been successfully used for studying the effect of carbon deposits at the length-scale of the active site.[19] Electron microscopy (EM) can visualize carbon deposits on length-scales from the single crystal[20–22] to the single catalyst particle[23] in two dimensions or carbon-based compounds in three dimensions.[24,25] Using soft X-ray scanning transmission X-ray microscopy (STXM) carbon formation can be mapped at sub-micron resolution and *in-situ* revealing distribution and, if combined with NEXAFS, speciation of carbon deposits on a solid catalyst.[26] Finally,

[a] Dr. M. Veselý, R. Valadian, Prof. E. T. C. Vogt, Prof. B. M. Weckhuysen, Dr. F. Meirer
Inorganic Chemistry and Catalysis, Debye Institute for Nanomaterials Science
Utrecht University
Universiteitsweg 99
3584 CG Utrecht (The Netherlands)
E-mail: b.m.weckhuysen@uu.nl
f.meirer@uu.nl
[b] L. M. Lohse, Dr. M. Toepperwien, Prof. T. Salditt
Institute for X-ray Physics
University of Göttingen
Friedrich-Hund-Platz 1
37077 Göttingen (Germany)
[c] Dr. K. Spiers, Dr. J. Garrevoet
Deutsches Elektronen-Synchrotron DESY
Notkestrasse 85
22607 Hamburg (Germany)
[d] Prof. E. T. C. Vogt
Albemarle Catalysts Company BV
Research Center Amsterdam
PO box 37650
1030 BE Amsterdam (The Netherlands)

Supporting information for this article is available on the WWW under https://doi.org/10.1002/cctc.202100276

confocal fluorescence microscopy (CFM) can visualize coke deposits in single crystals[27] or industrial-grade catalyst bodies[16,28] at micrometer resolution.

However, the volume that can be investigated by APT, EM, and soft X-ray STXM tomography is not sufficient to study a complete sub-millimeter catalyst body and CFM still offers limited spatial resolution and certainly limited information depth. Hard X-ray imaging techniques provide a similar spatial resolution as soft X-ray STXM[29–31] but the highest information depth of all above- mentioned techniques thus enabling 3-D studies[32–36] of, for example, metal distribution in the macro-pores[37] (pore sizes >50 nm) of an entire catalyst body[38–40] revealing the effect of those deposits on the catalyst's macro-pore space and accessibility. However, while this approach is very sensitive to metal deposits hard X-rays provide much weaker contrast for organic phases than soft X-rays because the energy dependent X-ray absorption is correlated with material density and atomic number.

Coke formation is an important factor in fluid catalytic cracking (FCC), which plays a crucial role in oil refinery industry[1,41] and converts high-molecular weight hydrocarbons to gasoline and propylene for polymer industry, with the recent promising trends to co-process biomass[41] and/or plastic waste as alternative sources of fuel.[42–44] Worldwide, approximately 350 FCC units are operated with an overall processing capacity of 14.7 million barrels per day and consuming 840,000 metric tons of FCC catalyst annually.[41,45] In each unit FCC catalyst particles with diameters between 50–150 μm experience 2500–10000 processing cycles with a 5000-cycle average. During each cycle the pre-heated feedstock is mixed with the (hot) catalyst at the bottom of the riser-reactor, in which a carbon-rich byproduct (coke) is formed due to cracking and pre-cracking of the feedstock molecules at the active sites of the catalyst. This type of coke is formed within the first 0.15 s after the catalyst entered the riser reactor,[46] while the residence time of a particle in the reactor is maximally five seconds per cycle. The catalyst particle also accumulates coke from unwanted dehydrogenation reactions on deposited poisoning metals (e.g., nickel and vanadium), additive aromatic coke from the feed deposited on the catalyst's outer surface, and coke formed during incomplete stripping.[3,5] These various coke deposits might cause different deactivation mechanisms and naturally vary in chemical nature. Based on product transient experiments[47] two mechanisms of FCC catalyst deactivation due to coke deposition have been proposed. In the first mechanism, at low coke contents, the active site of the catalyst material is covered by coke, which causes catalyst deactivation by preferential blocking of the strongest acid sites. In the second mechanism at high coke contents, pore-clogging causes reduced diffusion in micro-pores[48] (pore sizes <2 nm[37]) hindering mass transport of products and feedstock, in turn reducing catalyst efficiency.

With the aim to successfully tackle the challenge of visualization of weak absorbing organic phases by hard X-rays, we present here a unique characterization methodology to reveal, identify, and assess the effects of carbon deposits within single catalyst bodies at the macro-pore scale by using non-destructive, hard X-ray holotomography in differential contrast mode. We further combined this method with X-ray fluorescence (XRF) tomography data recorded for the same catalyst particle to reveal spatial correlations between coke deposits and structurally and/or chemically different regions in a commercially used FCC catalyst particle that was used as an archetypical example for a hierarchically complex porous catalyst body.

Our developed characterization methodology is summarized in Fig.1, which illustrates the complex workflow that integrates two synchrotron-radiation (SR) based X-ray holotomography experiments and one X-ray fluorescence (XRF) tomography performed at two different beamlines on the same sample. The imaged sample was a coked, used equilibrium catalyst (ECAT) catalyst particle of 60 μm in average diameter harvested from a batch taken from an industrial FCC unit. The sample was selected for its high coke content; by nature of the FCC process there is, on a single catalyst particle level, always inhomogeneity in the catalyst age, and thus the coke loading of individual catalyst particles. To ensure that the individual catalyst particle selected for this study was indeed a coked catalyst material, a particle was selected that appeared black in the optical microscope (Figure 1, Supporting Section S1). This single coked catalyst particle was then imaged by X-ray holotomography using a 64 nm pixel size resulting in a 3-D representation of the sample's electron density that was segmented into pore space and solid matter (see Experimental section). After imaging the coked catalyst material, the particle was placed in an in-house developed chamber for calcination of individual catalyst particles (Supporting Section S2) and calcined in air for 4 h at 600 °C using a 5 °C/min ramp to ensure removal of all carbon deposits in the catalyst without damaging the internal structure or causing any phase changes in the catalyst. This was confirmed by complementary lab-based powder XRD measurements of the same catalyst batch before and after calcination (Supporting Section S3) and by conducting an additional experiment: an ECAT catalyst batch (the same batch from which the individual catalyst particle was retrieved) was calcined during a synchrotron radiation (SR) based *in-situ* Small- and Wide-Angle Scattering measurement that was combined with a differential scanning calorimetry measurement (SAXS/WAXS/DSC). The results of this experiment confirmed stable crystallinity, pore broadening, and heat evolution during the calcination of the ECAT (see Supporting Section S4). After a cooling phase (5 °C/min ramp) the calcined particle was remounted and imaged again and the difference between the two X-ray holotomographies was used to obtain the 3-D coke distribution (differential contrast holotomography, see Figure 2, the Experimental section, Supporting Sections S5-S9, and Figure S5–S9).

Finally, we have combined these results with data from XRF tomography ($200\times200\times200$ nm^3 voxel size) recorded for the same calcined particle to investigate any spatial correlation between coke and specific metals present in the catalyst particle. Lanthanum stabilizes zeolite Y and is, in the brand of FCC catalyst particle used here, only present in the zeolite phase of the catalyst. It can therefore be used as a spectro-

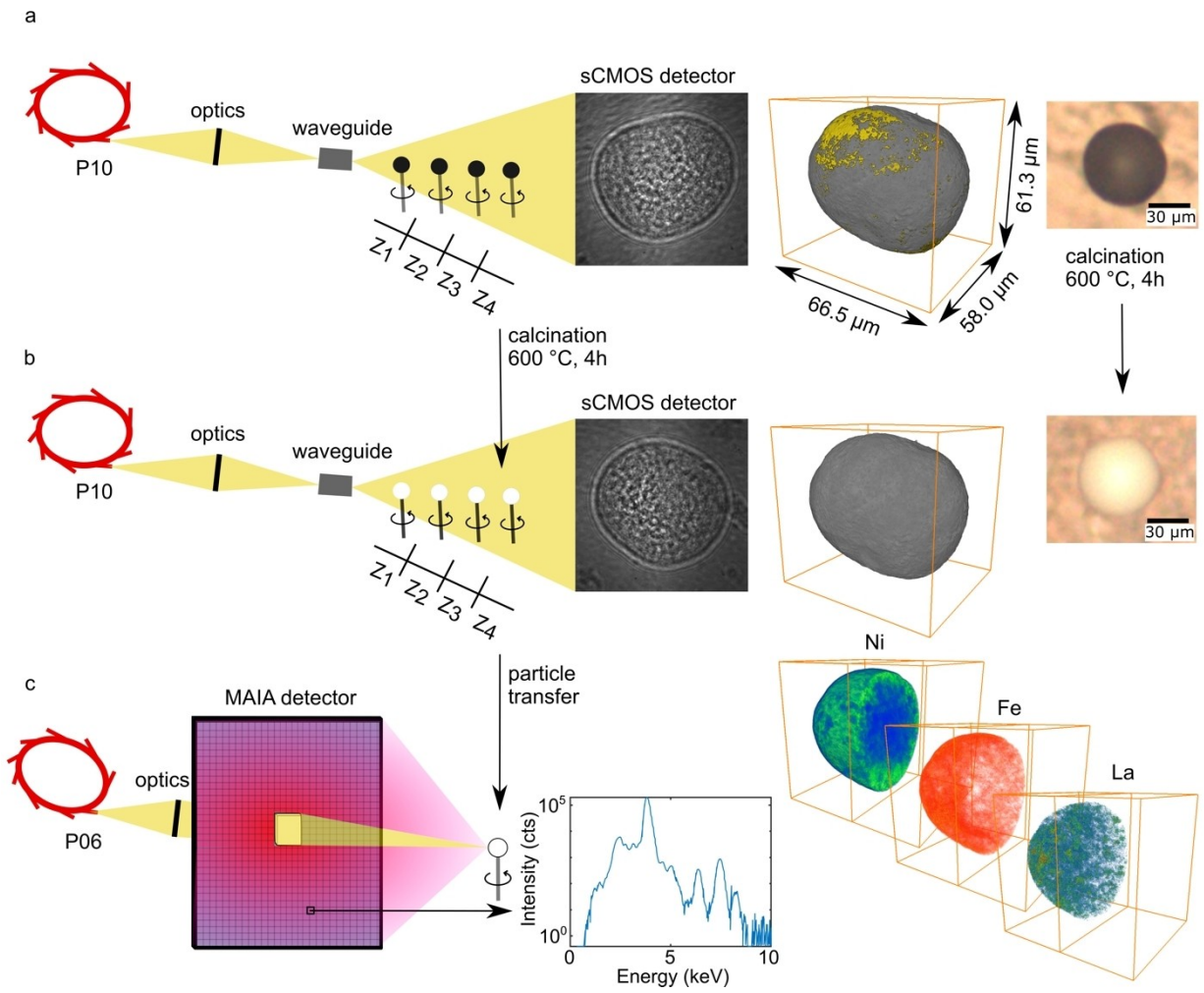

Figure 1. Experimental workflow and detection schemes. (a) In X-ray holotomography performed at beamline P10 of the PETRA III synchrotron, Kirkpatrick-Baez (KB) mirrors focus the X-ray beam generated by the synchrotron storage ring into a waveguide that creates a virtual point source with smoother illumination and smaller focus size, which is then used to image the FCC catalyst particle mounted on a carbon tip. Tomography was performed at four different distances between sample and a scintillator-based fiber-coupled sCMOS detector; see Experimental section for further details. (b) After the first measurement, the particle was calcined to burn off coke deposits. During this step the particle color changed from black to white evidencing the removal of the carbon deposits on the surface, while no other morphological changes took place (see Supporting Information). The particle was then re-mounted and measured again at beamline P10. (c) After this second X-ray holotomography the catalyst was also imaged by X-ray fluorescence (XRF) tomography at the PETRA III beamline P06. The emitted XRF was detected by means of a MAIA detector and XRF spectra were fitted to quantify the relative concentrations of the detected elements in every single pixel and at each projection angle (see Experimental section). In the final step the 3-D representations of the sample's electron density as well as the 3-D distribution of coke deposits (displayed as yellow surface deposits in (a)) had been reconstructed from X-ray holotomography, and the 3-D distribution of specific elements of interest was reconstructed from XRF tomography. The correlated X-ray holotomography and XRF tomography data are shown in Supporting Movie 1.

scopic marker for this most active component,[49–52] while iron and nickel are typical examples of poisoning metals, of which Ni is suspected to promote coke formation.[5] Figure 2 shows all the above-mentioned data processing steps including differential contrast holotomography and its correlation with XRF tomography. Figure 2 also emphasizes the nature of the differential contrast data, which is independent of the local phase of the catalyst. This means the carbon deposits in all solid phases (i.e., zeolite, aluminosilicate matrix, clay, iron, and nickel) and pores contribute to the difference in image contrast.

Solid-state ^{13}C NMR[3,12] methods previously distinguished two different carbon species, i.e., aromatic and aliphatic species, to be present in the ECAT FCC catalyst particle. This was confirmed by studying the effect of coke deposition during gas oil cracking (i.e., using a feedstock without carbon residue) and residue feedstock cracking (where the feedstock contained 4.3 wt.% of carbon residue).[53] While the coked catalyst that was used in gas oil cracking contained mainly aliphatic carbon, both aliphatic and aromatic carbon were found in the other case. The authors therefore suggested that catalytic cracking generates aliphatic carbon, while the main source of aromatic species is residual coke from the feedstock stream. However, these studies neither identified the spatial distribution of the carbon deposits within the catalyst particle (and therefore could not draw conclusions on their effect on e.g., the catalyst's pore space) nor considered the effect of poisoning metals. It is

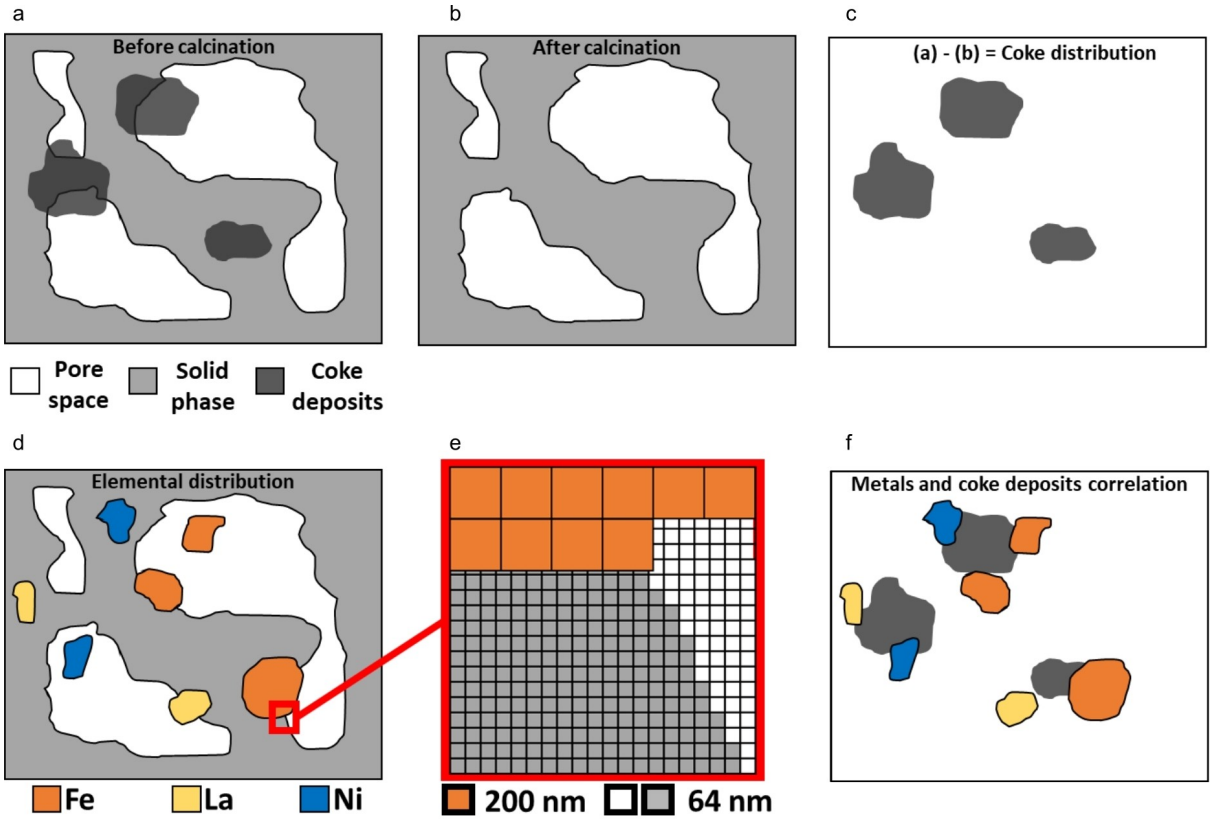

Figure 2. Schematic representation of the workflow of differential contrast X-ray holotomography combined with X-ray fluorescence (XRF) tomography. (a) Holotomography data before the calcination step. Here the coke deposits only contribute very little to the spatially resolved X-ray absorption resulting in very little contrast to resolve them (the contrast is artificially enhanced in the schematic for clarity). (b) X-ray holotomography data after the calcination step. These data are almost identical to (a) and show again the microstructure, but without the small absorption contribution of the carbon deposits. In (c), which is the difference image of the images (a) and (b) after registration, the spatial distribution of the carbon deposits is revealed. This method reveals carbon deposits in all solid phases of the catalyst as well as the pore space, that is, independent of their nature or location in the catalyst. Panel (d) displays a schematic overlay of holotomography data after the calcination step (b) and the corresponding metal distribution determined by XRF tomography. A zoom-in in (e) schematically depicts how these two data sets that have different voxel sizes ($200\times200\times200$ nm^3 voxel size for XRF data and $64\times64\times64$ nm^3 voxel size for holotomography data) have been registered. The difference in voxel size results in a smoother surface for carbon deposits and a rougher ('pixelated') surface for metals in the digital representation of the catalyst's microstructure. Panel (f) depicts how it was possible to study the spatial correlation between metals (from XRF tomography data) and carbon deposits (from X-ray holotomography data) in the FCC catalyst particle based on the complex registration of three independent 3-D tomography measurements of the same whole FCC catalyst particle.

known that both nickel and vanadium are active in hydrogenation-dehydrogenation reactions[5] and have therefore been suspected to increase coke selectivity.[54]

The only spatially resolved coke study we are aware of that identified carbon deposits in FCC catalysts used NRA line scans across particle cross-sections with a spatial resolution of several micrometers and revealed uniformly distributed carbon.[17] In a more recent study using NMR and EPR,[12] our group determined an approximate location of aromatic and aliphatic carbon deposits in FCC catalyst particles. Aliphatic coke was deposited within the particle, while aromatic coke was found predominantly in the outer part of the particle close to a paramagnetic species, such as iron (Fe^{3+}; d^5), nickel (Ni^{2+}; d^8) or vanadium (V^{4+}; d^1). However, NMR and EPR methods are not able to determine the 3-D spatial distribution of carbon deposits and their effect on the pore space inside a whole individual FCC catalyst particle. Although, the 3D distribution of metal deposits has been studied at tens of nanometers precision.[50]

Results and Discussion

Carbon deposits reduce accessibility and interconnectivity of the catalyst's pore network

The 3-D representation of the catalyst material obtained by X-ray holotomography was used to characterize the studied FCC catalyst particle using single particle metrics established previously[38,55] (Figure 3, Experimental Section, Supporting Tables S4 and S5 in Section S14). The good agreement with earlier work[38,50,55] confirms that a typical, i.e., representative, aged FCC catalyst particle was investigated and, in agreement with bulk XRD data and SR-based in-situ SAXS/WAXS/DSC measurements, the comparison of values before and after calcination confirms that no morphological changes other than coke removal took place.

The removal of coke deposits is also evident in the histograms of electron density recorded before and after calcination (Supporting Section S5). A small shift towards lower

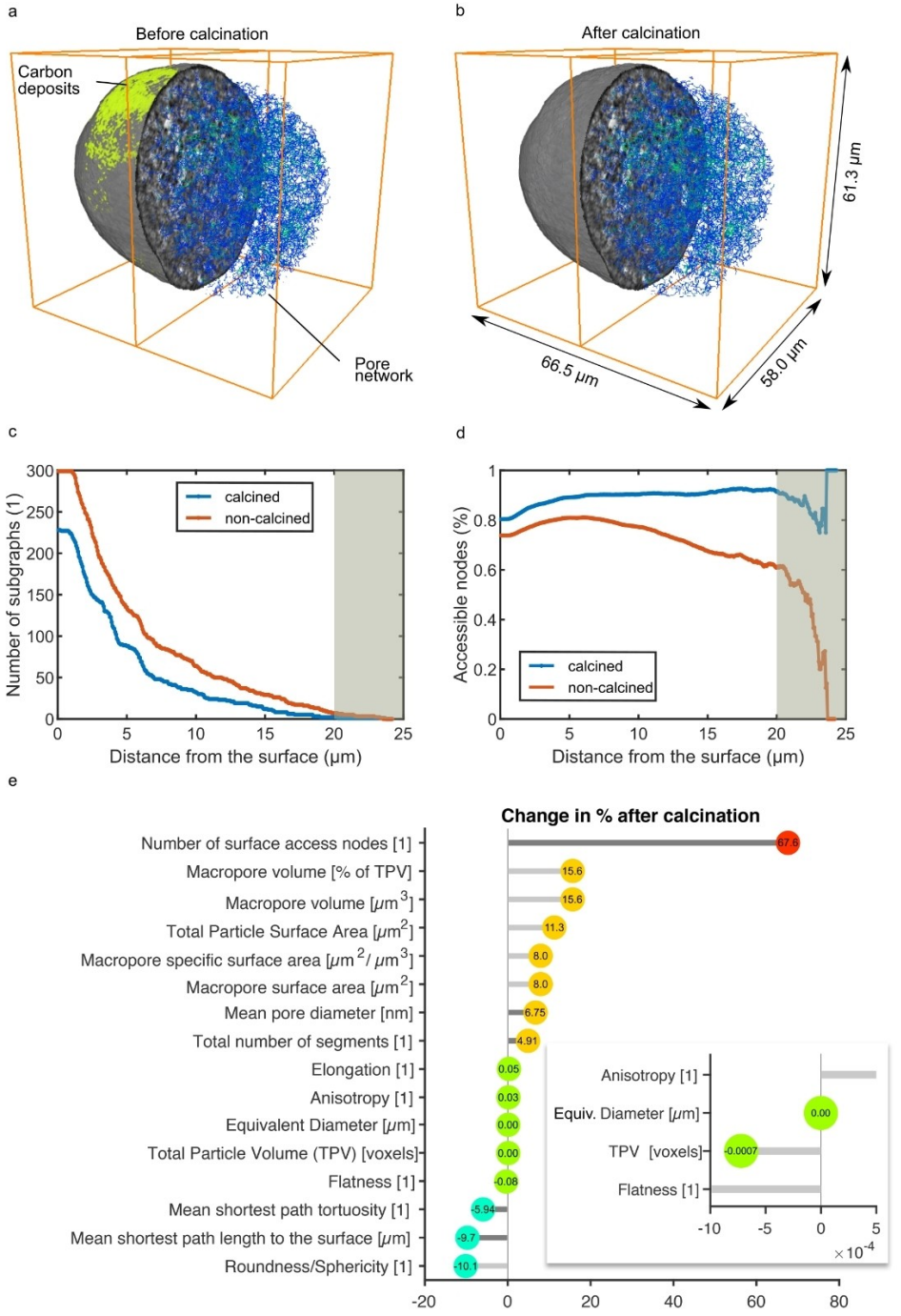

Figure 3. Effects of carbon deposits at the single catalyst particle level. (a, b) Virtual cut through the ECAT FCC particle before and after calcination as imaged by X-ray holotomography. The coke distribution is displayed in yellow-green. (c) The number of sub-graphs (isolated pore networks) of the pore network *versus* their distance from the particle surface shows that the largest number of sub-graphs was found within 2 µm from the surface, i.e. in the denser surface layer of FCC particles that contains more isolated cavities, especially in aged catalysts. Their number decreases towards the particle center, where porosity and pore connectivity increase, and the pore space is mainly represented by one large interconnected network. The number of sub-graphs decreased after calcination of the particle, evidencing that coke deposits indeed block macro-pores and isolate small pore volumes. The grey region indicates the statistically insignificant region which is related to the small number of voxels these shells that are close to the center of the particle. (d) The corresponding analysis of the accessibility of the nodes of the pore network as a function of their distance to the particle surface. (e) A comparison of single particle metrics (Experimental section, Tables S4-S5 in Section S14) before and after calcination confirms that no morphological changes other than a clear increase in accessible pore volume and a very small reduction (2655 voxels or 0.0072%) in the total particle volume took place indicating coke removal from the particle surface. Dark grey bars indicate values based on changes in the single particle pore network. All changes indicate how coke filled dips in the catalyst's surface, reduces accessibility via surface pore blockage and clogs macro-pores inside the particle. All reported values were established from the tomographic reconstruction of the single particle studied.

values of electron density is seen after calcination, which can only be caused by the removal of matter containing electrons. This is the basis for differential contrast holotomography that is, mapping the 3-D coke distribution as the difference between the two datasets. This also allowed segmenting the 3-D coke distribution into a set of voxels containing carbon deposits (Supporting Section S6). Next, we have estimated the total amount of coke in the catalyst particle to 2.37 vol.% (1.68 wt.% assuming the density of graphite), a value that was very close to typically reported amounts (0.7–1.5 wt.%)[5] for commercially used ECAT, and in excellent agreement with the 1.75 wt.% previously reported for ECAT with high carbon content,[12] confirming validity of our segmentation approach. We additionally confirmed this result by performing simultaneous thermogravimetric and differential thermal analysis combined with mass spectrometry to determine the amount of coke in the catalyst batch the single particle was taken from (Supporting Section S7). The results showed that the total weight loss caused by carbon deposits was 1.38 wt.%. This confirms that the individual particle selected from this batch was one with a high coke content.

Having both a 3-D representation of macro-pore space and coke distribution (Figure 3a,b) allowed investigating the effect of carbon deposits on the macro-pore network of the catalyst as previously done for metal deposits.[38,56] We have constructed two pore network models (one for the non-calcined and one for the calcined particle) that captured the connectivity of macro-pores by expressing them as a set of geometrical spatial graphs containing nodes (branching points) and segments (set of points connecting the nodes) with corresponding pore diameters for each node and segment point (see Experimental section, Supporting Section S8). The majority of nodes (almost 90%) of both networks were found interconnected, that is, in one graph (the 'main graph'), while other graphs ('sub-graphs') contained only few nodes covering just a small percentage of the particle's pore network. The observation that the main graph covers almost the entire pore network of an FCC catalyst particle is in line with previous work[38,57] and highlights the high degree of macro-pore interconnectivity. This interconnectivity is smaller before coke removal, as evidenced by the larger number of sub-graphs in the network of the coked particle (Figure 3c). In order to assess the accessibility of the macro-pores depending on their location in the particle we have determined the percentage of accessible nodes as function of their Euclidean distance from the particle surface (Figure 3d). The fraction of accessible nodes was higher for the calcined particle because the pore system became more interconnected and accessible.

The node accessibility in the network of the non-calcined FCC particle further continuously decreased towards the particle center indicating that coke deposits throughout the catalyst incessantly blocked macro-pores and caused lower pore connectivity. A comparison of the bulk properties of both pore networks is reported in Figure 3e and Supporting Table S1.

Here we want to emphasize two important advantages of our analytical approach and related data analysis: (1) the small difference in the mean pore diameter (7.4 nm) is statistically significant, independent of a much larger isotropic voxel size of 64 nm – this fact was thoroughly discussed in our previous papers.[38,50] (2) While the values reported in Figure 3e and Supporting Table S2 are based on a statistical evaluation of the networks our 3-D data allows pinpointing and visualizing the suggested pore clogging and path shortening for any specific macro-pore of the catalyst. As an example, Figure 4 and Supporting Movie 2 report the shortest paths between two arbitrarily chosen nodes (indicated by green and yellow circles) in both the calcined and non-calcined particle macro-pore networks highlighting the pore-clogging effect of coke.

We also evaluated the limited mass transport ability caused by carbon deposits by determining the effective permeability of the sub-volume displayed in Figure 4 (see Supporting Section S9, Table S2, Movie 3, and Reference 45 for further details).

The sub-volume's effective permeability increased from 132 nm^2 for the non-calcined FCC particle to 162 nm^2 for the calcined FCC particle, that is, the carbon deposits caused a 15.4% drop in the effective permeability. Moreover, the flow was found completely blocked along one axis. To visualize the effect of restricted mass transport in this sub-volume, the flow in the pore space along one principal axis was shown in Figure 4e (i.e., the non-calcined FCC particle) and Figure 4f (i.e., the calcined FCC particle). The shape and total number of streamlines demonstrate less restricted flow in the macro-pores of the calcined particle. The shape and total number of streamlines demonstrate less restricted flow in the macro-pores of the calcined particle.

The electron density of carbon deposits is correlated with their location in the catalyst particle

The example in Figure 4 shows that we were able to identify individual coke deposits in a whole catalyst particle. The analysis of separable and localized deposits or 'coke clusters' (Experimental section, Supporting Section S10, Supporting Movie 4) showed that the largest clusters are mainly located on the surface of the catalyst particle with the exception of one big cluster that was found close to the center of the catalyst particle, while smaller clusters (below volumes of 3 μm^3 or 10000 voxels) are distributed more homogeneously throughout the catalyst particle (Figure S8). Figure 5 shows a virtual cut through the particle indicating the individual carbon clusters located inside the catalyst particle (non-surface clusters shown in magenta) and at the surface (surface clusters shown in cyan). The separation also allowed inspecting the electron density values of surface and non-surface coke deposits reported as probability density functions for both types of coke (Figure S9). A clear increase of electron density in surface clusters shows the denser coke deposits at the surface of the particle. This observation of electron-denser carbon species being closer to the surface becomes obvious when plotting the mean electron density of the coke clusters as a function of distance to the particle surface (Figure 5c), which shows three distinct regions. The same plot including the standard deviation at each distance from the particle surface is reported in Figure S10 and shows a

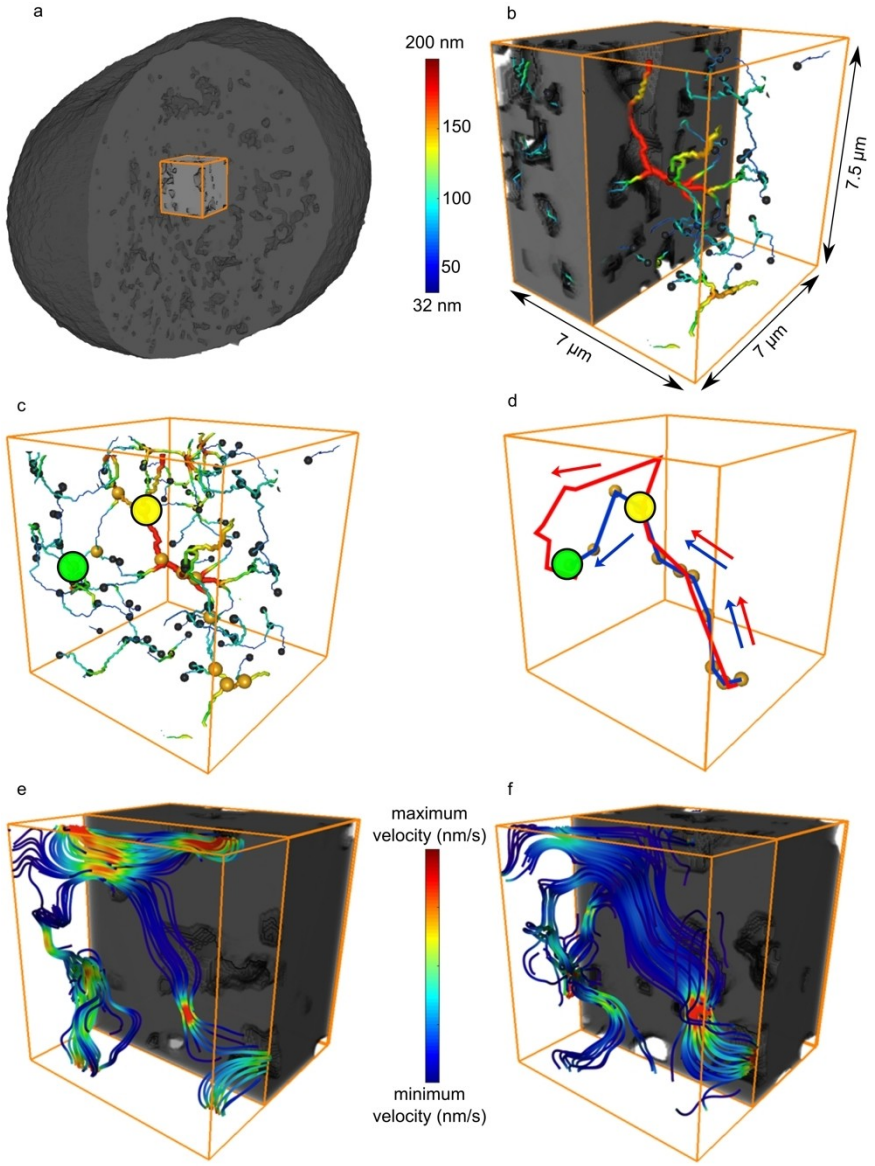

Figure 4. Pore blockage by carbon deposits within a catalyst particle. Specific example for pore narrowing and blockage inside the catalyst particle caused by the presence of carbon deposits. (a) Position of the sub-volume within the catalyst particle. (b) Zoom of the sub-volume displaying how the macro-pore volume is used to generate the pore network model with nodes (black spheres) and connecting segments. The color and thickness of the segments indicate the variation of the pore radius in every point of the pore network (not drawn to scale). In (c) the gold spheres indicate a specific path through the network that starts in the lower right part of the displayed volume and connects the nodes indicated by the yellow and green circles. This path indicates the shortest path between these two nodes in the calcined particle. This shortest connection is again highlighted in (d) by the blue path, which is shorter than the shortest path between these two nodes in the non-calcined particle (red path). This exemplifies how a path between two nodes of the pore network can be blocked by carbon deposits but is freed up after calcination (blue path). Panels (e) and (f) visualize this effect of pore blockage via the simulated mass flux based on a permeability calculation for the sub-volume along the (vertical) x-axis. The number, distribution and color of the streamlines (indicating normalized mass flow velocity) illustrate how mass flux is less restricted after coke removal in (f).

significantly larger variation of electron density closer to the surface. This larger variation clearly shows that 'surface coke' is more heterogeneous in terms of a different chemical nature (most probably represented by large polyaromatic species and aliphatic type species) and/or coke porosity than 'core coke', which is on average of lower electron density. The transient region between 'surface coke' and 'core coke' exhibits a linear decrease connecting high ('surface coke') and low coke electron density ('core coke') regions, which is also reflected in the corresponding probability density functions of electron density (Figure 5d). In agreement with literature,[3,12] this shift in electron density between 'surface coke' and 'core coke' can be assigned to the presence of large polyaromatic species and aliphatic type species, respectively. However, the 3-D packing of the same carbon species (coke porosity) within the catalyst particle can have the same effect and cause such a shift of the electron density. We can indeed imagine that the 3-D packing of carbon deposits could be denser at the outer surface of the catalyst

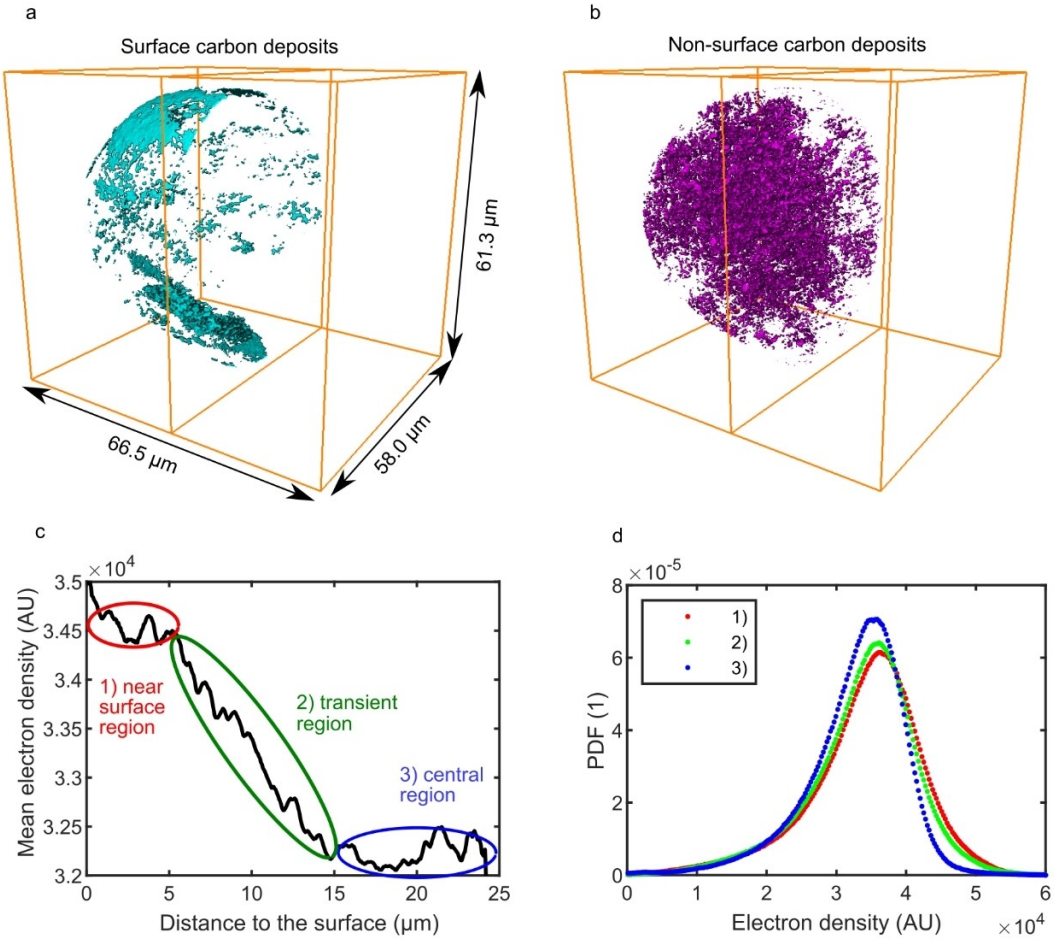

Figure 5. 3-D speciation of carbon deposits within a catalyst particle via electron density. (a) Virtual cut through the 3-D distribution of surface (cyan) and (b) non-surface (magenta) carbon deposits. Surface coke clusters are defined as clusters that contain at least one voxel that is located within 2 voxels from the particle's surface. In (c), the mean electron density value of all coke voxels (independent of whether they are classified as members of a surface or non-surface cluster) as a function of distance to the surface reveals three distinct regions: a near surface region, a transient region, and a central region. The corresponding probability density functions of these regions' electron density values are reported in (d) clearly showing the decreased electron density of coke deposits located in the center of the catalyst particle. The probability density functions (i.e., the histograms of the electron density values normalized by setting their integral to unity) were used to directly compare these histograms because the total number of voxels in near surface, transient, and central region is very different.

particle (i.e., less porous coke is present), as the packing is not limited by space restrictions. These results show that the developed differential contrast imaging is clearly sensitive enough for a tentative identification of small changes in electron density making the developed method more generally applicable to a wide range of catalytic reactions and systems.

Combining X-ray holotomography and X-ray Fluorescence tomography reveals the origin of coke

Figure 6 reports the radial distribution of coke, poisoning metals, and lanthanum, showing a much higher coke amount close to the particle surface, related to the patchy surface deposits of large polyaromatic coke species or denser coke packing. Both iron and nickel concentration profiles show the typical radial deposition profiles of poisoning metals in ECAT particles.[38,39,49,50,56,57] Their concentration is relatively higher close to the surface. Nevertheless, Ni can diffuse deeper into the particle due to its higher mobility compare to Fe. Therefore, Iron hotspots (region with highest Fe concentration) appears closer to the surface rather than Ni hotspots. This co-location of the highest concentrations of coke, Ni, and Fe is in line with the reported promotional effect of metals for coke formation[5] and/or the effect that metal transporting porphyrin-like species from the feedstock are co-deposited with the metals they carry. However, to quantify this effect we determined the total amounts of both surface and non-surface coke in the iron-, nickel-, and lanthanum-rich areas (Table 1).

To assess the domains' intrinsic average activity for non-surface coke formation the determined non-surface coke amount per domain was divided by the volume of the respective domain and expressed as percent of total activity. Note that activity here includes both accessibility and reactivity because the amount of non-surface coke formed per unit volume depends on both. Clearly, the La and Ni domains show

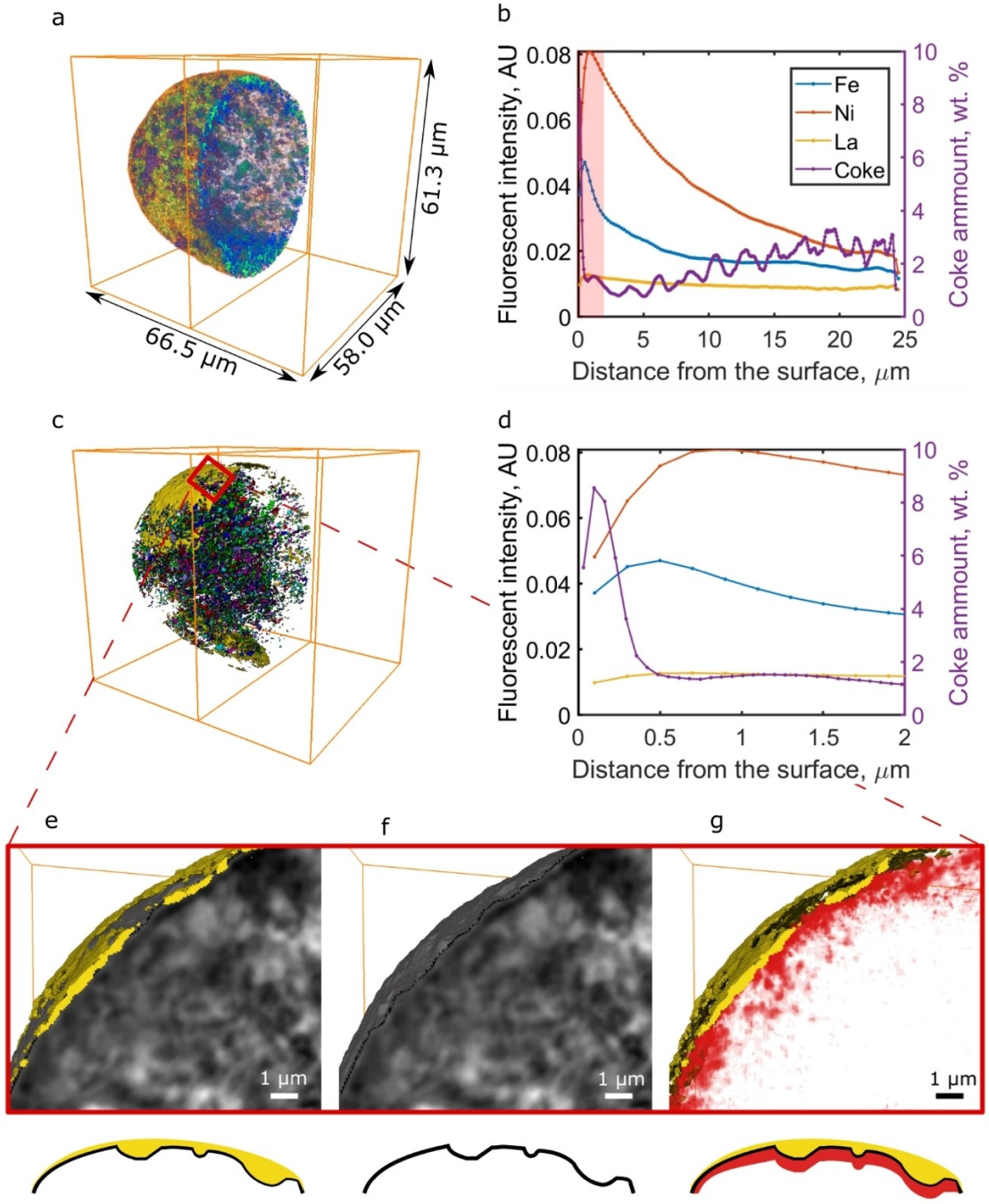

Figure 6. Correlated 3-D distributions of carbon deposits and metals within a single catalyst particle. (a) Virtual cut through the 3-D distribution of iron (yellow-red), nickel (blue-green), and lanthanum (magenta) as imaged by XRF tomography. The radial profiles in (b) report relative concentrations of iron, nickel, lanthanum (from XRF), and carbon deposits (from X-ray holotomography); the red region indicates the typical 1–2 µm thick surface region of decreased porosity. (c) 3-D distribution of individual carbon deposit clusters (individual clusters are plotted in different colors) identified by differential contrast holotomography. In (d) a zoom into the near surface region of the radial plot is displayed revealing the large amount of carbon deposited on the catalyst particle's surface. In (e) a zoom into the near-surface region of the catalyst particle is shown displaying the particle (X-ray holotomography, grey) and one of the large surface carbon deposit clusters (yellow). The comparison with panel (f) reveals how these patchy surface clusters smoothen the nodulated surface of the particle by filling dips and dents (see also the sketch below panels e–f). Panel (g) displays the 3-D Fe concentration distribution together with the surface cluster in the same sub-volume, showing that surface coke is located in close vicinity to the highest Fe concentrations found close to the surface of the catalyst particle (see also Supporting Movie 5). Note that, as this is a 3-D perspective image, the scale bar indicates the length correctly only in the plane of the virtual cut. This observation confirms a previous NMR study that suggested aromatic coke to be mainly in the near surface regions of the catalyst particle and close to a paramagnetic species, such as iron.[12]

significantly higher activity for the formation of non-surface coke than the Fe and metal-free areas. This is in line with the reported higher dehydrogenation activity of nickel[5,54] and the high density of active acid sites in the La-exchanged zeolites

Table 1. Absolute amounts of the two types of coke detected in metal-free as well as iron-, nickel-, and lanthanum-rich domains of the single catalyst particle. Metal-rich areas were defined via thresholding of the XRF data (see Methods section). The last column reports the normalized activity of those domains for non-surface coke formation. As expected, based on its proposed origin and location, surface coke (dominated by large polyaromatic species mainly transferred from the feed) was not found to be preferentially present in metal-rich regions of the catalyst particle: 85.16% of this coke was localized in metal-free domains. Non-surface, i.e., mainly aliphatic coke generated by cracking or hydrogenation reactions, showed a higher spatial correlation with metal-rich areas, but also in this case the majority, namely 78.86%, of this type of coke was localized in metal-free domains, that is, in the pores of the catalyst particle.

Domain	Total amount of surface coke [Vol.%]	Total amount of non-surface coke [Vol.%]	Normalized activity for non-surface coke formation [%]
Fe	6.11	3.56	17.9
Ni	4.86	8.81	21.2
La	6.62	11.19	46.4
Metal-free	85.16	78.86	14.5

that are the most active domains in the FCC catalyst particle for both cracking and coke formation,[58] which in turn confirms that non-surface coke is dominated by less dense aliphatic coke. Interestingly, only 28.8% of all individual La domains were found to contain coke. This also shows how the limited accessibility of the deactivated ECAT leads to the participation of less than a third of the zeolite domains in cracking reaction.

Conclusions

We have identified a carbon surface layer with a thickness of less than 1 μm filling dips and dents in the nodulated surface of an aged FCC catalyst particle (Figure 6). This is in line with suggestions from recent literature,[12] however, the analytical approach presented here not only provides clear evidence for this phenomenon, but further allowed for a detailed analysis of the effect of coke deposits in ECAT catalyst particles as well as a correlation between its nature and 3-D location. We show that the (electron) dense surface coke blocks a significant fraction of the macro-pores in the surface of the catalyst body hence severely limiting accessibility of the catalyst. A completely new observation from this study is that most (less electron dense) non-surface coke was found in the macro-pore space of the catalyst and it is interesting to note that the radial analysis of the coke distribution showed that higher amounts of coke are present in the core of the catalyst particle than in a region within ~1–10 μm from the surface.

This suggests that coke accumulates during multiple FCC cycles due to incomplete coke removal during regeneration caused by a limited average residence time in the regenerator unit (which is typically at the order of minutes).[41] During the time spent in this unit only coke in the regions close to the surface seems to be released –a process that is also influenced by the reduced mass transport ability of an aged FCC catalyst. This shows how the previously reported irreversible reduction in catalyst accessibility caused by metal poisoning has even more severe effects than previously assumed when investigating completely calcined FCC catalyst particles,[38,39,50,56,57,59] because incomplete coke removal leads to additionally reduced catalyst accessibility. We further show that Fe and metal-free areas show significantly lower activity for the formation of non-surface coke than the La (zeolite) and Ni domains, providing proof for the suggested higher dehydrogenation activity of nickel.[5,54]

These new insights lead to a further revision of our understanding of FCC catalyst ageing: while metal poisoning generally causes reduced porosity in the near surface regions of the catalyst, deposited Ni specifically increases coke formation. Incomplete coke removal during regeneration of the catalyst leads to accumulation of coke in the core of the particle blocking pores there. From the above it becomes clear that with the presented approach we have added a tool to the catalyst characterization toolbox that paves new ways for a more complete investigation of heterogeneous catalysts in its ability to visualize in 3-D both organic and inorganic phases in catalyst bodies of tens of microns at sub-200 nm 3-D resolution. In other words, the reported findings are not limited to FCC catalyst particles but can be used in a wide variety of catalytic reactions and systems.

Experimental Section

X-ray holotomography. The individual catalyst particle was examined using the X-ray holotomography setup GINIX (Göttingen Instrument for Nano-Imaging with X-Rays) installed at the P10 beamline at the PETRA III storage ring, DESY, Hamburg, Germany.[60] In order to account for missing information on specific spatial frequencies due to the zero crossings of the contrast transfer function,[61,62] describing the image formation for homogenous, weakly absorbing objects with a slowly varying phase, projections were acquired at four different source-to-sample distances. The total time needed for sample mounting and holotomography was approximately 4 h. The sample was roughly positioned in the X-ray beam using an optical microscope with a comparably large field of view, which was aligned with respect to the beam path. Fine adjustments of the sample position with respect to the center of rotation and the ultimate field of view were performed using the X-ray microscope. The experiments were carried out at an X-ray energy of 13.8 keV, which was achieved using a channel-cut monochromator. The X-ray beam was focused by a set of Kirkpatrick-Baez (KB) mirrors, leading to a focus size of approximately 300×300 nm^2. In order to reduce high-frequency artifacts caused by inhomogeneities on the mirror surface, as well as increase the coherence of the X-ray beam and reduce the focal spot size, a waveguide was placed in the focal plane of the KB mirrors.[60] The waveguide was formed by two crossed planar Mo/C/Mo thin films lamellae, each with 80 nm guiding layer. Approximately 5 m behind the sample, a scintillator-based fiber-coupled sCMOS detector with Gadox as scintillation material and a pixel size of 6.5 μm was placed (Photonic Science). Due to the divergent beam geometry, the setup comprises a large geometric magnification, leading to an effective pixel size of 64 nm in the sample plane. The individual coked catalyst particle was mounted on top of a graphite pin. The sample was placed at the four different source-to-sample distances and 1000 projection angles covering an angular range of 180° were recorded. Prior to phase retrieval with a CTF-based approach,[63] all projections were scaled to the same pixel

size and aligned to each other in Fourier space.[64] Tomographic reconstruction was carried out with the Matlab implementation of the filtered backprojection using a standard Ram-Lak filter. The resulting 3-D representation of the sample's electron density distribution was converted to 16-bit integer format and further processed by applying an anisotropic diffusion filter[65] and watershed segmentation[66] to determine pore and solid space. For image presentation, we used inverted grayscale colormap, i.e., the low electron density values appear as white pixels (voxels) and the high electron density values appear as black pixels (voxels).

Differential contrast holotomography. The subtraction of the electron density values of each voxel of the data set (the smallest volume unit in a 3-D data set) recorded before and after calcination shows regions where the electron density changed, i.e., the locations, where carbon was located before the calcination. Differential contrast holotomography is sensitive to any misalignment of the two subtracted data sets and also to differences in the achieved 3-D resolution. To ensure that the detected change in electron density was not due to artifacts caused by these effects the effective 3-D resolution of both data sets was estimated using Fourier ring correlation[67] (FRC; see Supporting Section S11 for further details) and found to be 179 nm and 189 nm for the non-calcined and calcined particle, respectively. Because the difference in the achieved 3-D resolution (10 nm) was found to be more than six times smaller than the used voxel size (64 nm) we conclude that any effect of differences in 3-D resolution is negligible. These values furthermore confirm the high reproducibility of the X-ray holotomography method. The second possible effect preventing a precise localization of coke deposits is a misalignment of the two data sets before subtraction. In order to achieve the best possible alignment of the two data sets a post-measurement image registration was performed, which was also necessary because the catalyst particle had to be mounted again on the pin manually in a light microscope after calcination and it is impossible to mount it in the exact same position as for the first measurement (before calcination). A careful two-step data alignment procedure was developed where in the first step a rough registration was performed using the total particle volumes (TPVs) of the two data sets. During the second step a fine alignment was carried out using the grayscale volume images of the recorded electron density refining the initial registration. More details about the registration procedure can be found in the Supporting Section S12. Since the result of volume subtraction is extremely sensitive to the registration procedure, we have calculated the precision of the registration using a scale-invariant feature transform[68] procedure (SIFT; see Supporting Section S13 for further details). The SIFT method determined local features of the sample's 2-D electron density distribution sampled in 9 virtual slices over the 3 principal axes through the aligned data sets. The obtained mean square displacement values were homogeneously distributed in space and had a mean value of 1.33 pixels. The histogram of the mean square displacement values is reported in Figure S14a, which shows that almost all displacement values are smaller or equal than 3.45 voxels - taking this as a very conservative estimate for registration and feature determination uncertainty we obtain 220.8 nm, implying almost perfect registration with an uncertainty close (i.e. within one voxel) to the limit set by the spatial resolution of the data set (189 nm or 2.95 voxels).

As discussed in previous work[38] the subtraction of the registered volume images leads to a volume image containing both positive and negative values. The negative values contain a contribution of noise and can be used to assess the noise level. The positive values contain contributions from noise and carbon deposits. To distinguish the carbon contribution from noise, we applied a statistical treatment supposing a Gaussian signal for noise that allowed determining an electron density threshold to identify carbon deposits (see Supporting Section S6). The identified amount of carbon deposits in the catalyst particle were expressed in weight percentage using the known mean density of FCC particles,[38] 2.957 g/cm^3, and graphite, 2.100 g/cm^3. The total amount of coke, 2.37 vol.% (1.68 wt.% assuming the sensity of graphite), was close to the value 1.75 wt.% previously reported for a commercial ECAT catalyst with high carbon content,[12] confirming the validity of the developed thresholding approach.

Single Particle Metrics And Porosity Profiles. Single catalyst particle studies have to rely on the fact that the sample under study is a representative example of the catalyst. We therefore determined a set of single particle metrics to establish that a typical aged FCC catalyst particle was studied (see Supporting Table S4 and S5). A comparison of these morphological parameters determined from the data recorded before and after calcination further confirms that almost no morphological changes other than changes in the accessible pore volume took place during calcination. The only change observed was that the total particle volume (TPV), which is defined as the volume of the particle including the pore space, decreased by a very small amount (2655 voxels or 0.0072 %) after calcination. The TPV includes the pore space and is therefore not sensitive to changes in pore space, hence this change was expected as it indicates that matter that absorbed X-rays before calcination was removed from the surface of the particle during coke removal. The fact that this change is so small indicates that only very little coke is actually deposited on the surface of the catalyst. When inspecting the 3-D distribution of coke deposits it further becomes clear that this effect is not likely caused by the noise level in the data, because the removed voxels are not randomly distributed over the whole particle surface (as one would expect if the removal was due to noise in the data) but clustered in patches filling dips and dents in the catalyst particle surface. This observation is confirmed by the significant increase of total particle surface area (defined as the surface of the particle not considering the pores) indicating a rougher surface after calcination, which is further supported by the roundness and sphericity parameters. The latter is a metric characterizing the particle's similarity to a perfect sphere (for which the roundness and sphericity parameters become one). The value before calcination confirms a smooth particle surface, which becomes rough after calcination – this again suggests that (patches of) coke deposits on the surface fill dips and dents in the catalyst's surface, which is in excellent agreement with earlier observations of a nodulated surface of aged (calcined) FCC catalyst particles.[38,39,55–57,59]

With respect to the observed porosity changes taking place due to calcination we observed a significant increase in macro-porosity and macro-pore surface area after the calcination step (Figure 3 and Supporting Table S4), which indicates that matter was removed also from the pores of the catalyst particle. Note that the measured porosity here inherently considered the previously reported metals contribution to pore space reduction[39,50,56,57] since the primary beam energy was above the metal's absorption edge. The mean pore diameter indicates narrower pores in the non-calcined particle, while the total number of segments designates a larger network, implying better interconnectivity of the pore space for the calcined particle. These changes support the idea that carbon deposits actually narrow (and also close) macro-pores. The parameters 'mean shortest path length' and 'mean shortest path tortuosity' are calculated as the average length and average tortuosity of the shortest path connecting every node of the pore network with the surface of the particle. This is a measure for a changing accessibility before and after calcination as it assesses a shortening or prolongation of the shortest diffusion path (i.e., a change in its tortuosity) from the surface to a node and vice-versa. Related to this but focused on pore clogging at the surface is the number of

surface access nodes that clearly shows how surface coke deposits significantly reduce the number of open macro-pores in the surface that provide access to the internal pore space of the catalyst.

To confirm the statistical significance of these single particle metrics and the evaluated porosity, we calculated these quantities also for another catalyst particle imaged at lower spatial resolution. Albeit recorded at lower resolution also for this different catalyst particle taken from the same sample batch all single particle metrics, as well as the porosity show the same trends in increased porosity and rougher particle surface after coke removal (see Supporting Section S14 and Table S4).

Pore Network Models. Pore networks were generated from X-ray holotomography data for both the calcined and non-calcined sample. Each network consisted of a set of geometrical spatial graphs containing nodes (branching points) and segments (set of points connecting the nodes) with corresponding pore diameters for each node and segment point. A graph is a set of connected points, while two graphs, although in the same network, are not connected. To compare the two pore networks before and after the calcination step, we have used the registered datasets and identical parameters for pore network generation (see Supporting Section S8 for more details). When comparing the pore-network before and after calcination the decrease in the number of sub-graphs reported in Figure 3c shows that macro-pore interconnectivity increased in the calcined particle. For both the calcined and non-calcined particle the majority of the small sub-graphs are located close to the surface, again in agreement with earlier work and in line with the observation of a lower macro-porosity in the surface of the particle, which causes lower pore interconnectivity there.[38,39,50]

Coke Cluster Analysis. To statistically evaluate coke deposits for the whole catalyst particle we have identified coke clusters in 3-D defined as a set of connected voxels containing coke and using a 6-connected neighborhood rule. In this step statistically insignificant clusters consisting of only 30 voxels or less have been treated as noise and removed. These small clusters contained only 0.27% of all voxels identified as coke. Then we analyzed the correlation between the size of the coke clusters and their Euclidian distance to the particle surface (Figure S8), which was calculated as the average value of all Euclidian distances of all voxels in the cluster. Note that we do not detect a continuous large coke layer covering the whole surface of the particle as might be expected from the optical microscopy image showing a completely black particle before calcination (Figure 1). The reason is that a layer that is significantly thinner than the resolution of our method cannot be detected.

The electron density values of surface and non-surface coke that are reported as probability density functions for both types of coke in Figure S9b show a clear shift towards surface clusters with higher electron density, i.e. carbon deposits on the surface of the particle have higher electron density. We conclude that the shift is caused by the different nature of carbon deposits in FCC catalysts: aliphatic and aromatic coke.[12] As discussed above it was suggested that during the FCC process aliphatic coke, which is created by the cracking reaction, is mainly deposited in the inner part of the catalyst particle, while aromatic coke, which has more electrons constituting the aromatic character and mainly originates from the feedstock stream, is preferentially deposited on the outer surface of the catalyst particle. The aromatic-aliphatic distribution we observe here therefore fully supports these previous findings.[12] These results further evidence the high sensitivity of the X-ray holotomography approach to assess subtle differences in electron density of carbonaceous species, which is in this case crucial to distinguish these two different types of carbon deposits. Here we want to point out that the probability density functions of the electron density displayed in Figure 5d show significantly overlapping values, indicating that both surface and non-surface coke consist of a mix of more and less dense coke, and does not imply the identification of specific molecular structures of hydrocarbon deposits. The histograms are further artificially broadened as an effect of the limited resolution of the technique: voxels that are not completely filled with coke, but only with a layer of coke that is thinner than the voxel size will appear as a voxel of lower coke electron density. However, because all coke clusters, including those on the surface, are generally thicker than one voxel (small insignificant coke clusters have been removed), the spatial probability distribution of not completely filled voxels is independent of their position in the inspected volume, i.e. we do not expect more or less not completely filled voxels in the surface or in the non-surface clusters. This is confirmed by the fact that the two probability density functions of the electron density have a very similar width: the effect of not completely filled voxels only broadens the probability density functions but does not affect their shift, i.e. the shift between the average electron density values of surface and non-surface coke species.

X-ray fluorescence tomography. To determine correlative 3-D distributions of the poisonous metals, such as iron and nickel, as well as lanthanum, which acts as a marker for the embedded rare-earth exchanged ultra-stable Y zeolites (RE-USY),[41] the catalyst particle was mapped using X-ray fluorescence (XRF) tomography. X-ray fluorescence tomography was performed at the P06 beamline, PETRA III using a primary photon energy of 15 keV and was focused to a 200 nm × 200 nm beam size by means of KB mirrors. A 200 nm × 200 nm raster scan step size was used resulting in a corresponding pixel size of 200 nm × 200 nm for each projection image. The sample was placed in the focal spot and raster scanned generating a point-by-point image. The X-ray fluorescence signal was detected using a 384-element Maia detector array.[69] We have used the same sample analyzed by X-ray holotomography placed on the same graphite pin. XRF tomography was accomplished by applying 120 projection angles covering 360°. This imaging strategy was successfully tested by our group[31] to minimize possible self-absorption effect in the ECAT FCC particle. The total time needed for sample mounting and tomography was 16 h. The collected XRF signal was processed using the GeoPIXE[70] software to fit the summed spectra and then to de-convolute each single pixel XRF spectrum in order to evaluate the relative concentration of the individual metals in 3-D. The resulting individual element specific XRF projection images were aligned and reconstructed using the iterative Algebraic Reconstruction Technique (i-ART) available within the TXM-Wizard software package.[71] The XRF resolution of 540 ± 180 nm was estimated based on edge line profiles; the method described in Section S11. Finally, the Avizo Fire software was used for image registration (alignment) of the reconstructed X-ray holotomography and XRF volume data, and 3-D image visualization. Note that although the XRF tomography and Holotomography resolution differ, we still can perform a proper spatial correlation as we thoroughly discussed in Supplementary information of the reference.[50] To identify and segment metal-rich domains within the catalyst particle the 3-D concentration distribution of Fe and Ni were thresholded by a value determined from the respective histograms of Fe and Ni single voxel concentrations. For La domain segmentation a different approach was used as La is only present in the zeolite domains and also because their average 2-D size is known from previous work on FCC catalyst particle cross-sections.[51] Therefore a 3-step segmentation was performed: (i) first a histogram-based thresholding was performed as before for Fe and Ni; next (ii) the local maxima of the La concentration were used as initial markers for separation of individual zeolite domains using (iii) a marker-based watershed segmentation utilizing the distance map calculated from the thresholded data in step (i). Then the

parameters used in steps (i-iii) were tuned to achieve the best agreement with literature reporting 2-D sizes between 0.52 μm^2 and 0.55 μm^2 for two different equilibrium catalyst (E-cat) particle cross-sections. In this way the final optimal domain size used for segmentation was found as 0.4938 μm^2.

Acknowledgements

We thank Dr. Marianna Gambino (Utrecht University, UU) and Dr. Matthias Filez (UU) for fruitful discussions, and Dr. Michael Sprung (DESY) for assistance during the experiments at DESY. Dr. Thomas Gaudisson (UU) is acknowledged for designing the calcination chamber. Dr. Andrei V. Petukhov (UU) is acknowledged for helping with the interpretation of the SAXS data. The work is supported by a Netherlands Organization for Scientific Research (NWO) VIDI Grant No. 723.015.007 (to FM) as well as by a NWO Gravitation program, Netherlands Center for Multiscale Catalytic Energy Conversion (MCEC) (to BMW). Parts of this research were carried out at a "beamline/facility" at DESY, a member of the Helmholtz Association (HGF). The research leading to this result has been supported by the project CALIPSOplus under the Grant Agreement 730872 from the EU Framework Programme for Research and Innovation HORIZON 2020. This research was supported in part through the Maxwell computational resources operated at Deutsches Elektronen-Synchrotron (DESY), Hamburg, Germany.

Conflict of Interest

The authors declare no conflict of interest.

Keywords: Fluid catalytic cracking · X-ray holotomography · carbon deposits · pore network · individual catalyst particle

[1] G. Ertl, H. Knözinger, F. Schüth, J. Weitkamp, Eds., *Handbook of Heterogeneous Catalysis*, Wiley-VCH, Weinheim, **2008**.
[2] J. Hagen, *Industrial Catalysis, A Practical Approach*, Wiley-VCH, Weinheim, **2008**.
[3] C. E. Snape, B. J. McGhee, J. M. Andresen, R. Hughes, C. L. Koon, G. Hutchings, *Appl. Catal. A* **1995**, *129*, 125–132.
[4] M. Guisnet, P. Magnoux, *Appl. Catal.* **1989**, *54*, 1–27.
[5] H. S. Cerqueira, G. Caeiro, L. Costa, F. Ramôa Ribeiro, *J. Mol. Catal. A* **2008**, *292*, 1–13.
[6] J.-O. Barth, A. Jentys, J. A. Lercher, *Ind. Eng. Chem. Res.* **2004**, *43*, 2368–2375.
[7] K. Qian, D. C. Tomczak, E. F. Rakiewicz, R. H. Harding, G. Yaluris, Cheng, X. Zhao, A. W. Peters, *Energy Fuels* **1997**, *11*, 596–601.
[8] A. Fonseca, P. Zeuthen, J. B. Nagy, *Fuel* **1996**, *75*, 1363–1376.
[9] A. Fonseca, P. Zeuthen, J. B. Nagy, *Fuel* **1995**, *74*, 1267–1276.
[10] A. Fonseca, P. Zeuthen, J. B. Nagy, *Fuel* **1996**, *75*, 1413–1423.
[11] S. R. Bare, F. D. Vila, M. E. Charochak, S. Prabhakar, W. J. Bradley, C. Jaye, D. A. Fischer, S. T. Hayashi, S. A. Bradley, J. J. Rehr, *ACS Catal.* **2017**, *7*, 1452–1461.
[12] D. Mance, J. van der Zwan, M. E. Z. Velthoen, F. Meirer, B. M. Weckhuysen, M. Baldus, E. T. C. Vogt, *Chem. Commun.* **2017**, *53*, 3933–3936.
[13] H. Shimada, M. Imamura, N. Matsubayashi, T. Saito, T. Tanaka, T. Hayakawa, S. Kure, *Top. Catal.* **2000**, *10*, 265–271.
[14] D. Espinat, H. Dexpert, E. Freund, G. Martino, M. Couzi, P. Lespade, F. Cruege, *Appl. Catal.* **1985**, *16*, 343–354.
[15] J.-O. Barth, A. Jentys, J. A. Lercher, *Ind. Eng. Chem. Res.* **2004**, *43*, 3097–3104.
[16] J. Ruiz-Martínez, I. L. C. Buurmans, W. V. Knowles, D. van der Beek, J. A. Bergwerff, E. T. C. Vogt, B. M. Weckhuysen, *Appl. Catal. A* **2012**, *419*, 84–94.
[17] D. A. Jacobs, G. C. Smith, R. D. Vis, A. F. H. Wielers, *J. Catal.* **1998**, *176*, 387–394.
[18] S. Mitchell, N.-L. Michels, K. Kunze, J. Pérez-Ramírez, *Nat. Chem.* **2012**, *4*, 825–831.
[19] J. E. Schmidt, J. D. Poplawsky, B. Mazumder, Ö. Attila, D. Fu, D. A. M. de Winter, F. Meirer, S. R. Bare, B. M. Weckhuysen, *Angew. Chem. Int. Ed.* **2016**, *55*, 11173–11177; *Angew. Chem.* **2016**, *128*, 11339–11343.
[20] J. E. Zuliani, T. Miyata, T. Mizoguchi, J. Feng, D. W. Kirk, C. Q. Jia, *Fuel* **2016**, *178*, 124–128.
[21] E. Tracz, R. Scholz, T. Borowiecki, *Appl. Catal.* **1990**, *66*, 133–147.
[22] J. R. Rostrup-Nielsen, in Catalysis: *Science and Technology Volume 5* (Eds.: J. R. Anderson, M. Boudart), Springer, Berlin, **1984**.
[23] M. Zbuzek, A. Vráblík, V. Tukač, M. Veselý, A. Prokešová, R. Černý, *Catal. Today* **2015**, *256*, 261–268.
[24] O. Orhan, E. Haffner-Staton, A. La Rocca, M. Fay, *Tribol. Int.* **2016**, *104*, 272–284.
[25] O. Ersen, J. Werckmann, M. Houllé, M.-J. Ledoux, C. Pham-Huu, *Nano Lett.* **2007**, *7*, 1898–1907.
[26] I. K. van Ravenhorst, C. Vogt, H. Oosterbeek, K. W. Bossers, J. G. Moya-Cancino, A. P. van Bavel, A. M. J. van der Eerden, D. Vine, F. M. F. de Groot, F. Meirer, B. M. Weckhuysen, *Angew. Chem. Int. Ed.* **2018**, *57*, 11957–11962; *Angew. Chem.* **2018**, *130*, 12133–12138.
[27] Q. Qian, J. Ruiz-Martínez, M. Mokhtar, A. M. Asiri, S. A. Al-Thabaiti, S. N. Basahel, B. M. Weckhuysen, *Catal. Today* **2014**, *226*, 14–24.
[28] G. T. Whiting, N. Nikolopoulos, I. Nikolopoulos, A. D. Chowdhury, B. M. Weckhuysen, *Nat. Chem.* **2019**, *11*, 23–31.
[29] F. Meirer, B. M. Weckhuysen, *Nat. Rev. Mater.* **2018**, *3*, 324–340.
[30] J. Reinhardt, R. Hoppe, G. Hofmann, C. D. Damsgaard, J. Patommel, C. Baumbach, S. Baier, A. Rochet, J.-D. Grunwaldt, G. Falkenberg, C. G. Schroer, *Ultramicroscopy* **2017**, *173*, 52–57.
[31] S. Baier, C. D. Damsgaard, M. Klumpp, J. Reinhardt, T. Sheppard, Z. Balogh, T. Kasama, F. Benzi, J. B. Wagner, W. Schwieger, C. G. Schroer, J.-D. Grunwaldt, *Microsc. Microanal.* **2017**, *23*, 501–512.
[32] J. Becher, D. F. Sanchez, D. E. Doronkin, D. Zengel, D. M. Meira, S. Pascarelli, J.-D. Grunwaldt, T. L. Sheppard, *Nat. Catal.* **2021**, *4*, 46–53.
[33] S. W. T. Price, D. J. Martin, A. D. Parsons, W. A. Sławiński, A. Vamvakeros, S. J. Keylock, A. M. Beale, J. F. W. Mosselmans, *Sci. Adv.* **2017**, *3*, e1602838.
[34] T. L. Sheppard, S. W. T. Price, F. Benzi, S. Baier, M. Klumpp, R. Dittmeyer, W. Schwieger, J.-D. Grunwaldt, *J. Am. Chem. Soc.* **2017**, *139*, 7855–7863.
[35] A. M. Beale, S. D. M. Jacques, E. K. Gibson, M. Di Michiel, *Coord. Chem. Rev.* **2014**, *277*, 208–223.
[36] A. M. Beale, S. D. M. Jacques, M. Di Michiel, J. F. W. Mosselmans, S. W. T. Price, P. Senecal, A. Vamvakeros, J. Paterson, *Phil. Trans. R. Soc. A.* **2018**, *376*, 20170057.
[37] J. Rouquerol, D. Avnir, C. W. Fairbridge, D. H. Everett, J. H. Haynes, N. Pernicone, J. D. F. Ramsay, K. S. W. Sing, K. K. Unger, *Pure Appl. Chem.* **1994**, *66*, 1739–1758.
[38] F. Meirer, S. Kalirai, D. Morris, S. Soparawalla, Y. Liu, G. Mesu, J. C. Andrews, B. M. Weckhuysen, *Sci. Adv.* **2015**, *1*, e1400199.
[39] J. Ihli, R. R. Jacob, M. Holler, M. Guizar-Sicairos, A. Diaz, J. C. Silva, D. F. Sanchez, F. Krumeich, D. Grolimund, M. Taddei, W.-C. Cheng, Y. Shu, A. Menzel, J. A. Bokhoven, *Nat. Commun.* **2017**, *8*, 809.
[40] P. Sprenger, T. L. Sheppard, J.-P. Suuronen, A. Gaur, F. Benzi, J.-D. Grunwaldt, *Catalysts* **2018**, *8*, 356.
[41] E. T. C. Vogt, B. M. Weckhuysen, *Chem. Soc. Rev.* **2015**, *44*, 7342–7370.
[42] S. L. Wong, N. Ngadi, T. A. T. Abdullah, I. M. Inuwa, *Ren. Sust. Energy Rev.* **2015**, *50*, 1167–1180.
[43] G. Lopez, M. Artetxe, M. Amutio, J. Bilbao, M. Olazar, *Ren. Sust. Energy Rev.* **2017**, *73*, 346–368.
[44] Y. Wang, Y. Cao, J. Li, *Renewable Energy* **2018**, *124*, 34–39.
[45] R. Sadeghbeigi, *Fluid Catalytic Cracking Handbook*, Elsevier, Amsterdam, **2012**.
[46] M. A. den Hollander, M. Makkee, J. A. Moulijn, *Catal. Today* **1998**, *46*, 27–35.
[47] Y. Schuurman, C. Delattre, I. Pitault, J. P. Reymond, M. Forissier, *Chem. Eng. Sci.* **2005**, *60*, 1007–1017.
[48] Y. S. Zhang, X. Lu, R. E. Owen, G. Manos, R. Xu, F. R. Wang, W. C. Maskell, P. R. Shearing, D. J. L. Brett, *Appl. Catal. B* **2020**, *263*, 118329.
[49] S. Kalirai, U. Boesenberg, G. Falkenberg, F. Meirer, B. M. Weckhuysen, *ChemCatChem* **2015**, *7*, 3674–3682.

[50] Y. Liu, F. Meirer, C. M. Krest, S. Webb, B. M. Weckhuysen, *Nat. Commun.* **2016**, *7*, 12634.
[51] S. Kalirai, P. P. Paalanen, J. Wang, F. Meirer, B. M. Weckhuysen, *Angew. Chem. Int. Ed.* **2016**, *55*, 11134–11138; *Angew. Chem.* **2016**, *128*, 11300–11304.
[52] M. Gambino, M. Veselý, M. Filez, R. Oord, D. F. Sanchez, D. Grolimund, N. Nesterenko, D. Minoux, M. Maquet, F. Meirer, B. M. Weckhuysen, *Angew. Chem. Int. Ed.* **2020**, *59*, 3922–3927.
[53] S. Haitao, D. Zhijian, Z. Yuxia, T. Huiping, *Catal. Commun.* **2011**, *16*, 70–74.
[54] C. A. Trujillo, U. N. Uribe, P.-P. Knops-Gerrits, L. A. Oviedo, P. A. Jacobs, *J. Catal.* **1997**, *168*, 1–15.
[55] S. R. Bare, M. E. Charochak, S. D. Kelly, B. Lai, J. Wang, Y. K. Chen-Wiegart, *ChemCatChem* **2014**, *6*, 1427–1437.
[56] F. Meirer, D. T. Morris, S. Kalirai, Y. Liu, J. C. Andrews, B. M. Weckhuysen, *J. Am. Chem. Soc.* **2015**, *137*, 102–105.
[57] F. Meirer, S. Kalirai, J. N. Weker, Y. Liu, J. C. Andrews, B. M. Weckhuysen, *Chem. Commun.* **2015**, *51*, 8097–8100.
[58] M. Guisnet, P. Magnoux, D. Martin, in *Stud. Surf. Sci. Catal.* (Eds.: C. H. Bartholomew, G. A. Fuentes), Elsevier, Amsterdam, **1997**, pp. *1–19*.
[59] F. Krumeich, J. Ihli, Y. Shu, W.-C. Cheng, J. A. van Bokhoven, *ACS Catal.* **2018**, *8*, 4591–4599.
[60] T. Salditt, M. Osterhoff, M. Krenkel, R. N. Wilke, M. Priebe, M. Bartels, S. Kalbfleisch, M. Sprung, *J. Synchrotron Radiat.* **2015**, *22*, 867–878.
[61] P. Cloetens, W. Ludwig, J. Baruchel, D. Van Dyck, J. Van Landuyt, J. P. Guigay, M. Schlenker, *Appl. Phys. Lett.* **1999**, *75*, 2912–2914.
[62] S. Zabler, P. Cloetens, J.-P. Guigay, J. Baruchel, M. Schlenker, *Rev. Sci. Instrum.* **2005**, *76*, 073705.
[63] L. D. Turner, B. B. Dhal, J. P. Hayes, A. P. Mancuso, K. A. Nugent, D. Paterson, R. E. Scholten, C. Q. Tran, A. G. Peele, *Opt. Express* **2004**, *12*, 2960–2965.
[64] M. Guizar-Sicairos, S. T. Thurman, J. R. Fienup, *Opt. Lett. OL* **2008**, *33*, 156–158.
[65] P. Perona, J. Malik, *IEEE Trans. Syst., Man, Cybern.* **1990**, *12*, 629–639.
[66] F. Meyer, *Signal Process.* **1994**, *38*, 113–125.
[67] M. van Heel, M. Schatz, *J. Struct. Biol.* **2005**, *151*, 250–262.
[68] D. G. Lowe, in *Proceedings of the Seventh IEEE International Conference on Computer Vision*, **1999**, pp. *1150–1157*.
[69] U. Boesenberg, C. G. Ryan, R. Kirkham, D. P. Siddons, M. Alfeld, J. Garrevoet, T. Núñez, T. Claussen, T. Kracht, G. Falkenberg, *J. Synchrotron Radiat.* **2016**, *23*, 1550–1560.
[70] C. Ryan, D. Cousens, S. Sie, W. Griffin, *Nucl. Instrum. Methods Phys. Res. Sect. B* **1990**, *49*, 271–276.
[71] Y. Liu, F. Meirer, P. A. Williams, J. Wang, J. C. Andrews, P. Pianetta, *J. Synchrotron Radiat.* **2012**, *19*, 281–287.

Manuscript received: February 22, 2021
Accepted manuscript online: March 4, 2021
Version of record online: March 31, 2021